Combustion and Flame 190 (2018) 1–11

Contents lists available at ScienceDirect

Combustion and Flame

journal homepage: www.elsevier.com/locate/combustflame

Near-field flame dynamics of liquid oxygen/kerosene bi-swirl injectors at supercritical conditions

Xingjian Wang*, Yixing Li, Yanxing Wang, Vigor Yang*

School of Aerospace Engineering, Georgia Institute of Technology, Atlanta, GA 30332, USA

ARTICLE INFO

Article history:
Received 29 June 2017
Revised 7 August 2017
Accepted 4 November 2017
Available online 23 November 2017

Keywords:
Supercritical combustion
Bi-swirl injector
Liquid oxygen/kerosene combustion
Geometric effect
Thermal protection
Flame stabilization

ABSTRACT

The flame dynamics of liquid bi-swirl injectors are numerically investigated using the large eddy simulation technique. Liquid oxygen (LOX) and kerosene at subcritical temperatures are injected into a supercritical pressure environment. The theoretical framework is based on the full conservation laws and accommodates real-fluid thermodynamics and transport theories over the entire range of fluid states. Turbulence/chemistry interaction is modeled with a laminar flamelet library approach, the validity of which is demonstrated in the present work. The near-field flow and flame characteristics are carefully studied. The flame is anchored in the wake of the inner injector post by two counter-rotating vortices, and further stabilized by center and corner recirculation zones in the downstream region. Differences in the flow patterns between the cold-flow and combustion cases are recognized. Various geometric parameters, including recess region, post thickness, and kerosene annulus width, are examined in depth to explore their influence on flame characteristics. A recess region is found to be necessary to achieve efficient mixing and combustion. The absence of a recess region increases the penetration depth of the kerosene stream in the downstream region and reduces the thermal protection provided to the injector faceplate. On the other hand, a thicker LOX post or a wider kerosene annulus protects the faceplate more efficiently, and introduces larger recirculation zones near the LOX post surface and thus higher flow residence time to better anchor the flame. However, the flame attachment for thicker post and wider annulus induces a stronger heat flux to the post surface, and thus increases the risk of thermal failure of the injector device. The dynamic characteristics of the flame field are also discussed. The flow oscillations within the injector are found to be dominated by a quarter acoustic wave, while the oscillatory field near the injector exit is characterized by vortex shedding. The characteristic frequency of the vortex shedding is similar for different LOX post thicknesses and annulus widths, and is determined by the exit velocity profiles.

1. Introduction

This paper deals with the combustion characteristics of bi-swirl injectors of liquid oxygen (LOX) and kerosene under supercritical conditions typical of contemporary rocket engines. Figure 1 shows schematically the injector considered in the present study, which mimics the bipropellant injectors used in the RD-0110 engine [1]. LOX and kerosene are tangentially introduced into the inner and outer swirlers, respectively. The centrifugal force induces the LOX film to flow along the solid surface of the inner swirler and form a thin liquid sheet, which exits and impinges onto the surrounding kerosene stream in the recess region. The interaction of LOX and kerosene determines the quality of subsequent mixing and combustion process.

Swirl is widely adopted to achieve efficient mixing and combustion in gas-turbine [2,3] and liquid-propellant rocket engines [4,5]. Understanding of the flow and flame dynamics of swirl-stabilized gas turbine combustors has been significantly improved with the implementation of large eddy simulation (LES) over the last few decades [6–9]. Studies of swirl injectors in rocket engines, however, are much less documented. Rocket engines, especially those for the first-stage or booster applications, operate at much higher pressures, often exceeding the critical pressures of propellants, a situation known as supercritical conditions [10]. Such extreme operating conditions pose severe challenges to experimental diagnostics and numerical simulations. Several theoretical [4,11] and numerical studies [12,13] have been conducted to explore various underlying mechanisms dictating flow instabilities in swirl injectors.

Numerous experimental studies have been performed to examine the effects of injector geometry and flow conditions on mixing and combustion characteristics [14–18]. It has been found that an elevation in the chamber pressure increases the liquid film

* Corresponding authors.
E-mail addresses: xwang343@gatech.edu (X. Wang), vigor.yang@aerospace.gatech.edu (V. Yang).

https://doi.org/10.1016/j.combustflame.2017.11.007
0010-2180/

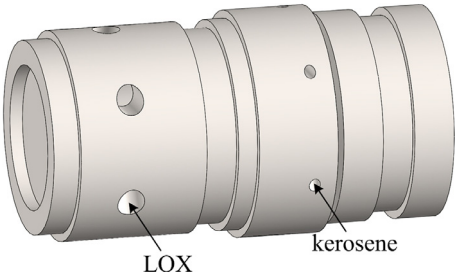

Fig. 1. Bi-swirl injector of liquid oxygen and kerosene.

thickness but decreases the spreading angle [19,20]. Ahn and coworkers [21,22] studied the effect of recess length and pressure on combustion characteristics at both subcritical and supercritical pressures. The discharge coefficient was found to increase with chamber pressure, and decrease with increasing recess length. The presence of a recess region facilitates the interaction of propellants and enhances mixing efficiency. As the recess length increases, the mixing pattern gradually shifts from external to internal mode, improving the propellant interaction and combustion performance.

These investigations provide valuable data, but are not sufficient to gain direct insight into the underlying physics. In particular, optical diagnostics currently available for use in the flame zone do not enable detailed examination of the detailed flow and flame evolution, and especially the flame stabilization mechanisms. The fundamental processes driving combustion instabilities are still not well understood. Other important injector attributes, such as post thickness and annulus width have also not been experimentally examined. A comprehensive study, considering more geometric parameters, is needed to obtain high-fidelity representation of injector flow and combustion dynamics.

An alternative approach is to use advanced numerical tools to illuminate the detailed structures and flow dynamics in swirl injectors. Direct numerical simulations (DNS) resolve all turbulent scales and steep gradient layers, but they are restricted to simple flows with low Reynolds numbers and low density ratios [23,24], and become computationally prohibitive for practical devices with complex geometries and high Reynolds number flows. Although there are still many unresolved issues in modeling unclosed subgrid-scale (SGS) motions [25,26], the LES technique has been widely employed to simulate practical systems at supercritical pressures [27–30], resulting in good agreement with existing experimental data, and is thus employed in the present study.

Wang and Yang [31] recently conducted an LES-based numerical investigation of the combustion characteristics of LOX/kerosene bi-swirl injectors at supercritical conditions, and revealed for the first time the flame stabilization mechanism. The kerosene annulus width was found to significantly affect the flow evolution, and increasing the width may introduce unstable burning in the annulus. Wang et al. [32] explored the effects of injector geometries, including recess length, LOX post thickness, and annulus width, on the LOX/kerosene mixing characteristics. A larger post thickness or annulus width was found to lead to a higher spreading angle of the LOX film and more efficient intersection with the kerosene stream, thereby facilitating propellant mixing in the recess region. Improved mixing efficiency, however, does not guarantee better injector performance; the thermal load on the post surface may increase and in consequence reduce the injector life.

The present paper investigates the flame dynamics of liquid bi-swirl injectors under various geometric conditions using the LES technique. A laminar flamelet approach is implemented to model turbulence/chemistry interaction. The flow and flame evolution in the injector near field is explored extensively. The differences in the flowfield under conditions with and without combustion are examined systematically. The paper is structured as follows: Section 2 summarizes the theoretical and numerical framework; Section 3 describes the numerical setup and flow conditions; and Section 4 presents the results and detailed discussion.

2. Theoretical and numerical formulation

The theoretical basis of the present study is described in Oefelein and Yang [33], which deals with supercritical fluid flows and combustion over the entire range of fluid thermodynamic states of concern. Turbulence closure is achieved using the LES technique. The Smagorinsky eddy viscosity model proposed by Erlebacher et al. [34] is employed to represent the effects of SGS motions. Thermodynamic properties, including density, enthalpy, and specific heat at constant pressure, are evaluated based on fundamental thermodynamic theories and the modified Soave–Redlich–Kwong (SRK) equation of state (EOS) [10]. Transport properties, including thermal conductivity and dynamic viscosity, are estimated using an extended corresponding-state principle. Mass diffusivity is obtained by the Takahashi method calibrated for high-pressure conditions [35]. The evaluation of thermodynamic and transport properties has been validated and implemented in previous studies [10,36–38].

Note that filtering EOS produces an unclosed SGS term, which appears to be negligible for ideal gases and is assumed to be insignificant for most real-gas LES simulations. However, several studies [25,39,40] have shown that this SGS term may be substantial in regions of steep property gradients. Several SGS models were proposed through a priori analysis of the DNS non-reacting database. The extension of the SGS models to reacting flows is, however, still an open question. An alternative approach is to tabulate thermochemistry with a presumed subgrid probability density function (PDF) [41,42], but this has not been thoroughly examined for LES-based simulations. Because of these uncertainties, adding an existing EOS SGS model to the current framework would not necessarily improve the numerical results. Therefore, the filtered density is directly evaluated using the filtered pressure, compressibility factor, and temperature (i.e., $\tilde{\rho} = \tilde{p}/\tilde{Z}\tilde{R}\tilde{T}$). Modeling of the SGS term and its impact on the filtered density should be explored in the future.

Modeling of turbulence/chemistry interaction remains a critical issue, and an accurate and efficient treatment is yet to be established, even for ideal-gas mixtures. The situation is more challenging for real fluids in the transcritical regime because of thermodynamic nonidealities and transport anomalies [10]. In the present study, both LOX and kerosene are injected at subcritical temperatures and become supercritical in the flame zone. A precise classification of turbulent diffusion flame regimes is still an open question, because diffusion flames do not have well-defined length, time, and velocity scales [43]. The local flame scales depend on local flow conditions. The chemical kinetics of kerosene combustion involve hundreds of species and thousands of elementary reaction steps, rendering direct simulation of detailed chemistry computationally prohibitive.

A steady laminar flamelet model is implemented in the present study. The underlying assumption is that the local Damkohler number ($Da = \tau_f/\tau_c$) is sufficiently large and the chemistry is sufficiently fast to follow the flow changes; τ_f and τ_c denote the local flow time and chemical time, respectively. Unsteady effects and flame extinction occur when Da is low. A priori study showed that the local strain rate in the current flowfield is much smaller than the extinction strain rate ($\sim 10^7$/s at 100 atm) for oxygen/kerosene counterflow diffusion flames [38]. This implies that Da is sufficiently large in the present study to justify the validity of the flamelet model. Instead of solving species transport equations, which encounter stiffness issues due to the range of chemical time

scales, the flamelet model solves the following transport equation for the mixture fraction, along with the mass, momentum, and energy equations,

$$\frac{\partial \rho f}{\partial t} + \frac{\partial (\rho u_j f)}{\partial x_j} = \frac{\partial}{\partial x_j}\left(\rho D \frac{\partial f}{\partial x_j}\right) \tag{1}$$

In the LES formulation, filtering Eqn. (1) yields an unclosed term representing the subgrid scalar flux ($\Phi_j^{sgs} = \bar{\rho}(\widetilde{uf} - \tilde{u}\tilde{f})$), which is modeled with an eddy viscosity model. Provided the filtered mixture fraction, the variance of the mixture fraction, and the scalar dissipation rate from the turbulent field, the species mass fractions are retrieved from the pre-calculated library. The beta-function distribution is assumed for the filter PDF of the mixture fraction. The expressions of the mixture fraction variance and the scalar dissipation rate can be found in Ref. [29].

A three-component surrogate of kerosene [44], n-decane/n-propylbenzene/n-propylcyclohexane (74%/15%/11% by volume), has shown good agreement with jet-stirred reactor data and is thus employed. A skeletal mechanism with 106 species and 382 reactions developed by Wang et al. [45] is implemented in the present study because of its computational efficiency and high accuracy in predicting global combustion characteristics in a pressure range of 1–20 atm and an equivalence ratio range of 0.5–1.5. Further validation is required to determine whether this skeletal mechanism is suitable at higher pressures. The solutions of counterflow diffusion flames are used to build the flamelet library, which contains the filtered species mass fractions from a set of equilibrium solutions over a range of strain rates of concern at a pressure identical to that of the current LES simulations. Flame solutions are obtained using Chemkin [46]. Because kerosene combustion at high-pressure, low-temperature conditions is numerically difficult to converge, special treatment was used to ensure convergence. A convergent solution is first computed at room pressure, and then rescaled according to the correlation between the flame thickness and the product of pressure and strain rate [38]. The rescaled solution, treated as the initial solution at high pressures, improves the convergence dramatically. The species mass fractions are filtered by convoluting them with the joint PDF of the mixture fraction and scalar dissipation rate and stored in the library.

The numerical framework is based on a preconditioning scheme and a unified treatment of general-fluid thermodynamics [47]. It employs a density-based, finite-volume methodology, along with a dual-time-step integration technique [48]. Temporal discretization is achieved using a second-order backward difference, and the inner-loop pseudo-time term is integrated with a four-step Runge–Kutta scheme. Spatial discretization is obtained using a fourth-order central difference scheme in generalized coordinates. Fourth-order matrix dissipation, developed by Swanson and Turkel [49], is employed to ensure numerical stability and minimum contamination of the solution. Finally, a multi-block domain decomposition technique associated with the message passing interface technique of parallel computing is applied to optimize computation speed.

3. Injector configuration and flow conditions

Figure 2 shows a longitudinal sectional view of the injector with six tangential inlets for LOX and kerosene, respectively. Here, r and x denote the axial and radial coordinates, respectively. R_v, R, Δr, h, and l represent the radius of the vortex chamber, radius of the nozzle, width of the kerosene annulus, LOX post thickness, and recess length, respectively. The initial ambient pressure (p_0) is 100 atm, which is well above the critical pressures of both oxygen and kerosene. The injection temperature for LOX and kerosene is 120 and 300 K, respectively, so both LOX and kerosene undergo a transcritical change from compressed-liquid to supercritical state in the downstream region. Strong property gradients exist when

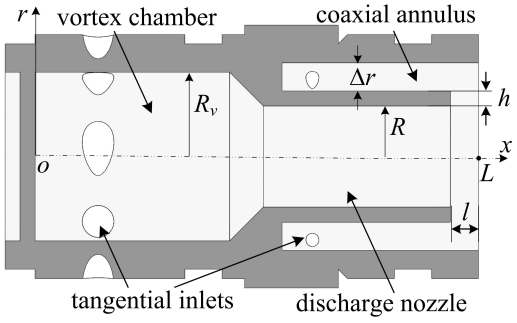

Fig. 2. Longitudinal section of bi-swirl injector.

they cross the pseudo boiling line (fluid transition region), where the grid refinement is enforced to ensure the convergence of the numerical solver. The mass flow rates of LOX and kerosene are 0.15 and 0.065 kg/s, respectively. The radii of the vortex chamber (R_v) and discharge nozzle (R) are fixed at 4.5 and 2.7 mm, respectively. The Reynolds number based on the baseline post thickness (0.8 mm) and exit velocity profile is about 1.2×10^5.

The computational domain includes the injector interior (8.4R in the axial direction) and a downstream region (25R and 8R in the axial and radial directions, respectively). Because of the tremendous computational cost of simulating the flame evolution in the entire three-dimensional (3D) region, only a cylindrical sector with periodic boundary conditions specified in the azimuthal direction is treated. This leads to the neglect of flow variations in the azimuthal direction and the exclusion of the vortex-stretching mechanism responsible for turbulent energy transfer from large to small eddies. In spite of these limitations, previous studies have shown that the present method is able to capture many salient features of supercritical flows, including density stratification, interfacial instability, and real-fluid effects [12,36,50]. The predicted spreading angle and liquid film thickness show good agreement with classical theory. To further elucidate, a full 3D simulation of the baseline configuration was performed for the non-reacting case and compared with the current axisymmetric results. Note that it is much more computationally expensive and numerically challenging for the current framework to perform 3D combustion simulation of the liquid–liquid injection system at supercritical conditions.

Figure 3 shows the simulated distributions of the kerosene mass fraction for axisymmetric and 3D configurations. Similar flow structures are observed in the recess region, where kerosene covers the upper surface and the LOX post surface, and a shear layer between kerosene and LOX enhances the mixing. These structures are important for flame initiation and thermal protection as will be discussed later. The axisymmetric case does not provide good prediction of the kerosene mass fraction near the centerline ($r/R = 0$), because of the absence of dynamics in the azimuthal direction. This appears not to be an issue for the combustion case, because a diffusion-dominated flame separating the LOX and kerosene prevents kerosene transporting to the centerline. The bottom of Figure 3 also shows the flow at different cross-sectional views. The non-axisymmetric structures become prominent when the flow convects downstream. A 3D combustion study should be conducted in the future to capture the transverse flow instabilities.

The no-slip boundary condition is applied at the injector surface. Because of the inherently large Reynolds number of the flow, resolving the complete law of the wall would be extremely computationally expensive. The first grid size along the wall exceeds the length of the viscous sublayer and the van Driest damping function is employed to scale the mixing length near the wall. Because

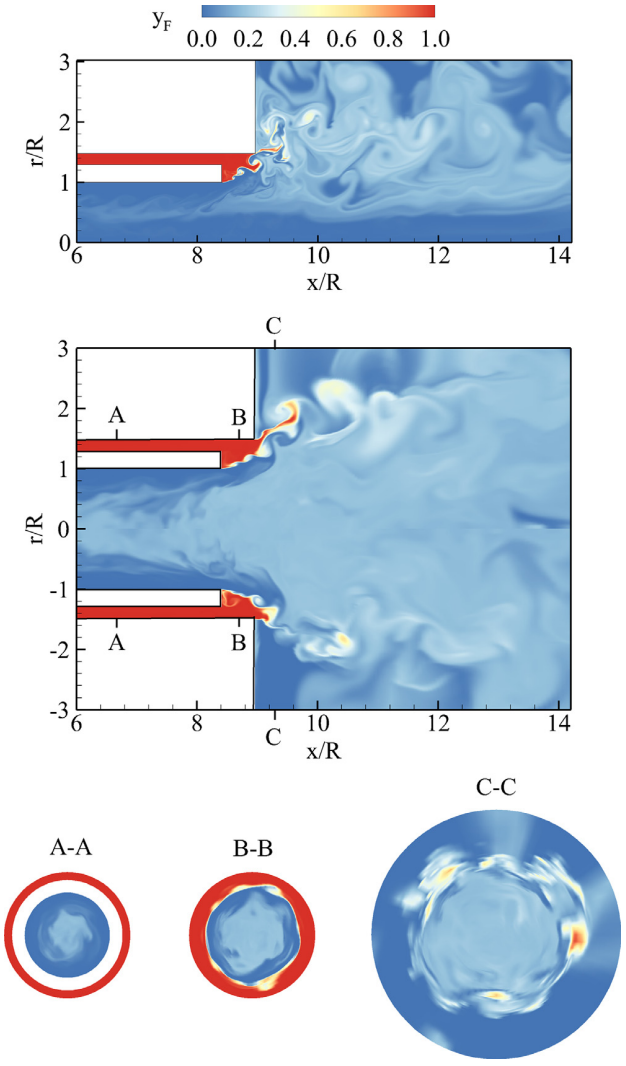

Fig. 3. Comparison of the kerosene mass fraction for non-reacting axisymmetric (top) and 3D (middle and bottom) simulations.

of the lack of wall temperature profiles, the injector surface is assumed to be adiabatic. This of course differs from a practical rocket injector, in which intensive cooling is supplied to the injector surface to prevent overheating. A non-adiabatic surface might change the flame anchoring point slightly. At the inlets, the azimuthal and radial velocities are determined from the given mass flow rate and swirl strength. The pressure is obtained from the radial momentum equation. At the downstream boundary, non-reflecting conditions based on the characteristic equations proposed by Li et al. [51] are applied to avoid undesirable wave reflection by extrapolation of primitive variables from the interior region. A reference pressure is applied to preserve the average pressure in the computational domain.

4. Results and discussion

While there is insufficient experimental data available for direct validation of the present model for liquid bi-swirl injectors, previous studies [29,52] have shown that the theoretical/numerical framework employed here is capable of tackling general fluids in both the sub- and super-critical regimes. The grid resolution in the present paper was selected based on a grid independence study conducted previously [31]. The total number of grid points is 1.6 million for the current axisymmetric configuration. The grid refinement is enforced near the injector surface and in the regions of steep gradients, including near-wall regions, the LOX/gaseous core mixing layer, and the LOX/kerosene mixing layer. The smallest grid size is 2 μm, compared to the Taylor scale of 8.4 μm. In a previous cold-flow study [32], the geometric parameters, including the recess region, LOX post thickness, and kerosene annulus width, were found to play significant roles in determining the injector flow behaviors. It is thus necessary to explore whether and how these parameters affect combustion characteristics. Table 1 summarizes the geometries of the four cases used in the current combustion study; these are identical to those used in the previous cold-flow study [32]. Case I, with a recess length of 1.5 mm, is the baseline. The recess region is removed in Case II; the post thickness increases to 1.3 mm in Case III; and the kerosene annulus increases to 1.0 mm in Case IV. The following sections will first discuss the flow and flame structures for the baseline and then analyze the geometric effects on the combustion characteristics through comparisons of the four cases.

Table 1
Geometric parameters for four cases.

Case number	Annulus width (Δr, mm)	Post thickness (h, mm)	Recess length (l, mm)
I	0.5	0.8	1.5
II	0.5	0.8	0.0
III	0.5	1.3	1.5
IV	1.0	0.8	1.5

4.1. Baseline flame dynamics

Because both LOX and kerosene are injected at subcritical temperatures, autoignition is unlikely to occur. The temperature from the flamelet library that acts like a heat source is introduced to the flowfield and initiates the chemical reactions when the mixing develops sufficiently in the downstream region. The calculation was performed for a long enough period (10 ms) for each simulation with a time step of 10^{-4} ms. Data are accumulated and analyzed after the flowfield has reached its statistically stationary state ($t \geq 2$ ms).

Figure 4 shows the instantaneous distributions of flow properties, including temperature (T), mixture fraction (Z), density (ρ), axial velocity (u_x) and mass fraction of H_2O (y_{H2O}) for the baseline case. Liquid propellants emanating from the tangential inlets mix and combust in the recess region. The flame is highly wrinkled by shear-layer instability in the downstream region. Hot combustion products reverse the flow direction near the centerline and flow back into the injector interior, preheating the LOX stream in the inner swirler. The evolution of the liquid films in the inner and outer swirlers resembles its counterpart in the cold-flow environment [32]. The LOX stream flows along the wall, constrained by the swirl-induced centrifugal force, and this leads to the formation of a thin liquid film and a central gaseous core. The surface of the LOX stream undergoes small-amplitude oscillation, due to hydrodynamic instabilities. In the outer swirler, the kerosene stream fills the whole annulus and becomes fully developed before leaving the annulus. The high amplitude of axial velocity near the injector exit implies strong expansion of gaseous products.

Figure 5 shows the radial distributions of time-averaged density, temperature, and velocity components near the injector exit. In the kerosene annulus, the distributions of temperature and density are uniform, and the axial and azimuthal velocities exhibit fully-developed profiles. In the inner swirler, however, non-uniform property distributions are observed. The axial velocity becomes negative for $r/R < 0.63$ because of the center-recirculating

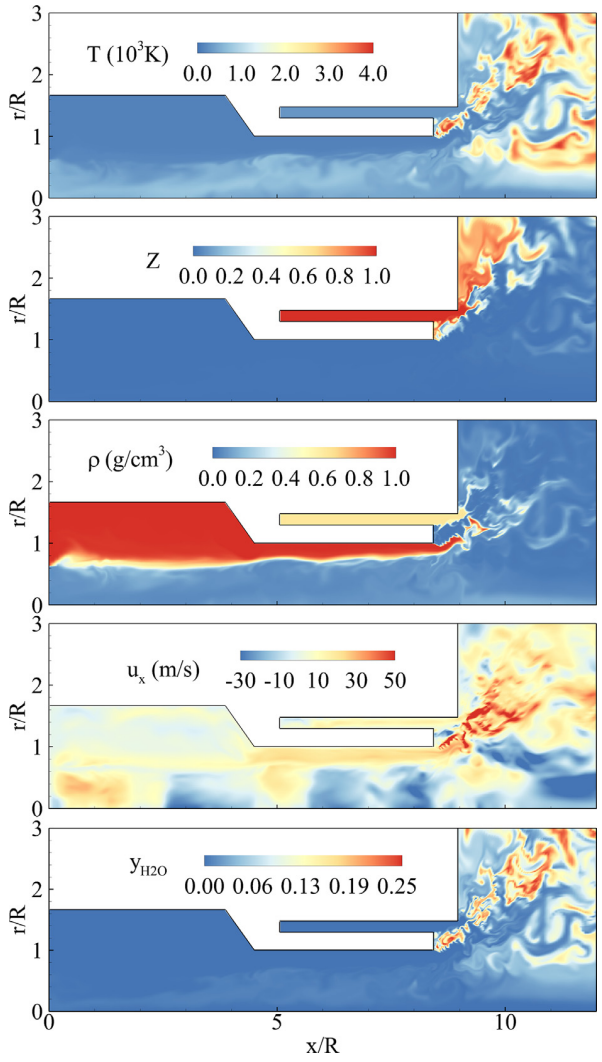

Fig. 4. Instantaneous distributions of temperature, density, mixture fraction, axial velocity, and H_2O mass fraction for the baseline (Case I).

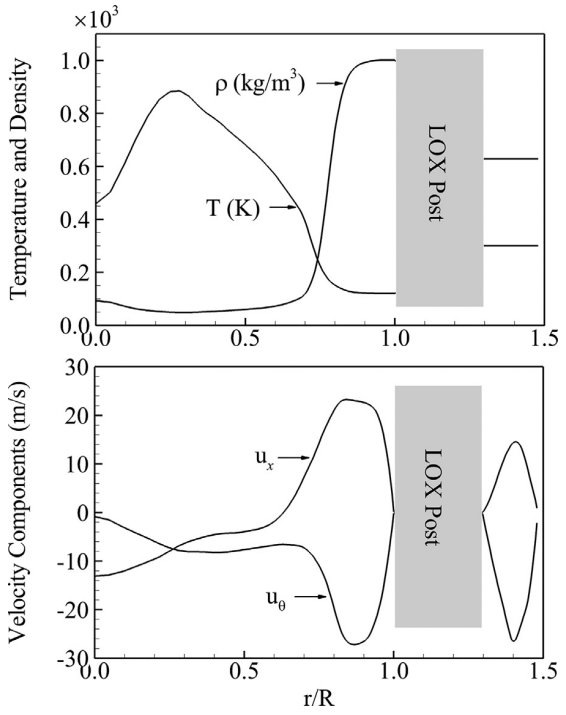

Fig. 5. Radial distributions of time-averaged density, temperature, and axial and azimuthal velocity components near the injector exit ($x/R = 8$).

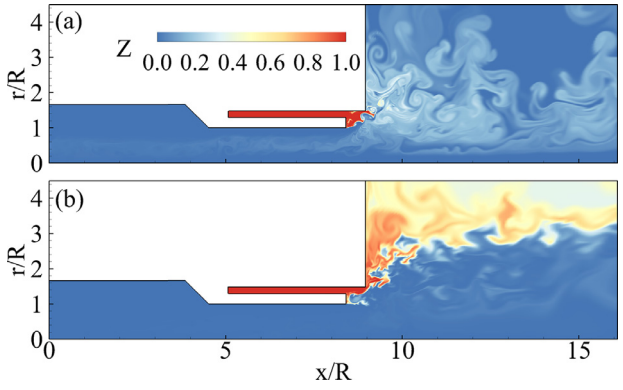

Fig. 6. Comparison of instantaneous distributions of mixture fraction for (a) cold-flow and (b) combustion cases.

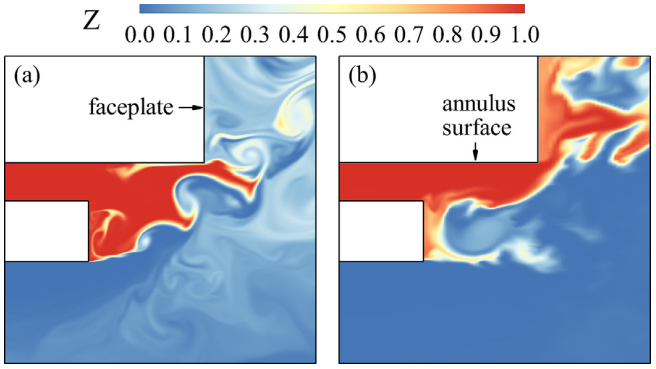

Fig. 7. Zoomed-in view of distributions of the mixture fraction for (a) cold-flow and (b) combustion cases at the injector exit.

flow downstream of the injector. The gaseous core, with an initial temperature of 300 K, heats up to 900 K through the reversal flow containing hot combustion products. The temperature gradually decreases to a subcritical value (120 K) at the wall along the radial direction, indicating a transcritical change of fluid state. Accordingly, the oxygen density varies smoothly from a liquid-like state to a gas-like state as the distance from the wall increases.

Figure 6 shows the snapshots of the mixture fraction for the cold-flow and combustion cases. The occurrence of chemical reactions introduces significant difference in the reactant distributions in the recess and its downstream regions. In the combustion case, kerosene and LOX are separated by the wrinkled flame. In the cold-flow case, a mixture of kerosene and oxygen is developed and transported downstream, and part of it is recirculated into the gaseous core in the injector. Figure 7 shows a zoomed-in view of the mixture fraction field downstream of the injector post for the two cases. A kerosene-rich mixture resides in the recess region in a broader area for the cold-flow case, and intensive propellant mixing is achieved through turbulent mixing and diffusion. In the combustion case, the hot products generated in the flame expand in all directions, causing the kerosene to flow further along the annulus outer surface and the injector faceplate in the down-

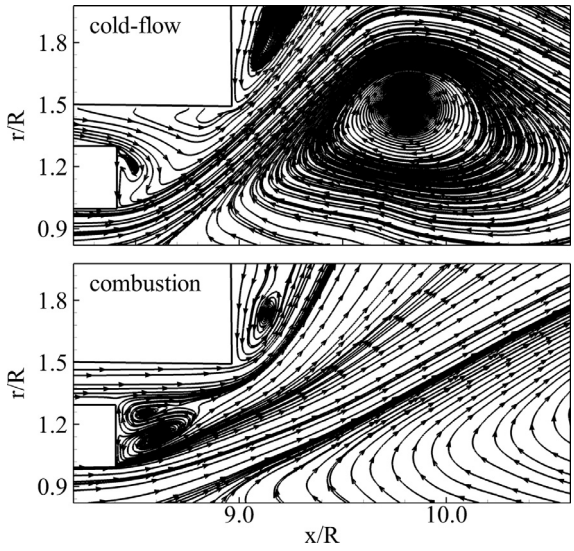

Fig. 8. Time-averaged streamlines in the near field of the inner swirler exit: cold flow (top) and combustion cases (bottom).

stream region. A thin film of the kerosene-rich mixture forms on the rear-facing surface of the LOX post.

Figure 8 shows the time-mean streamlines of the two cases. A small recirculating zone containing kerosene forms near the upper part of the LOX post tip for the cold-flow case. Because the momentum flux of the LOX in the inner swirler is about five times that of the kerosene in the outer swirler, the outward spreading of the LOX film blocks the kerosene stream, which turns its flow direction and is entrained by the LOX film, occupying a major part of the recess region. The mixing of the two propellants always begins in the recess region and reaches the desired level a short distance downstream. For the combustion case, however, two counter-rotating recirculating zones are produced in the recess region. These zones contain hot products and provide the primary flame-holding mechanism. The outward spread of the LOX stream decreases, and the center recirculation zone is pushed to a region further downstream, with its center at $x/R = 11.8$, as compared to 9.81 for the cold-flow case.

It is important to explore whether the flame can be sustained in the recirculating region in Fig. 8b. Two important time scales are discussed here: flow residence time τ_f and ignition time delay τ_{ign}. The flame is considered to be sustainable in the recess region if the flow residence time is larger than the ignition time delay. The former can be estimated as the turbulent mixing time using the length (l_f) and velocity (u_f) scales of the recirculating region. The length scale is best described by the post thickness, $l_f = h$, and the velocity scale is estimated as $u_f = u_o - u_k$, where u_o and u_k represent the mean velocities of oxygen and kerosene at the injector exit, 15.46 and 8.76 m/s, respectively in the present case. Therefore, the flow residence time is obtained by,

$$\tau_f = \frac{l_f}{v_f} = \frac{h}{u_o - u_k} \tag{2}$$

The estimated τ_f is 0.1 ms, which is about one half of the ignition time delay (0.2 ms) for kerosene/oxygen combustion in a perfectly stirred reactor at 1000 K and 100 atm. The ignition time delay decreases by three orders of magnitude ($\sim 10^{-4}$ ms) if the initial temperature reaches 1600 K, but it increases exponentially when the initial temperature decreases. Therefore, combustion would not occur if the cold reactants mix without imposition of a heat kernel. If a heat source is added in the recess region, ignition takes place within a flow residence time. Such an ignition kernel resides

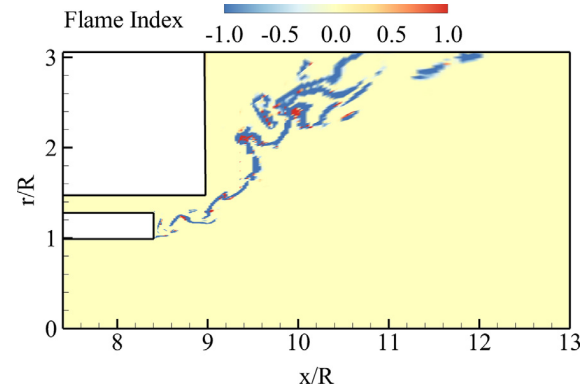

Fig. 9. Instantaneous distribution of flame index in the injector near-field and downstream region.

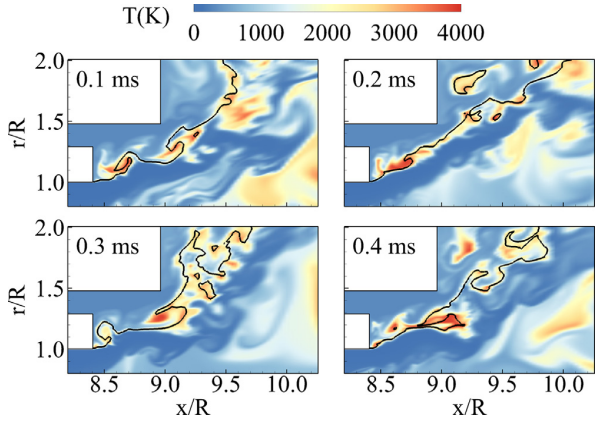

Fig. 10. Temporal evolution of the flame field. (Solid curves denote stoichiometric surfaces).

in the recirculating region, consumes incoming reactants from the inner and outer swirlers, and becomes self-sustained. It also preheats the reactants that convect and combust in the downstream region. The convection time (τ_c) from the entrance of the recess region to the injector exit is estimated as

$$\tau_c = l/\bar{u} \tag{3}$$

Substitution of l with 1.5 mm and $\bar{u}$ with 12.1 m/s gives a convection time of 0.12 ms. The center and corner recirculating zones behave like a hot-product pool, such that the LOX and kerosene streams are heated to above 1000 K with a reduced ignition delay time. Intensive burning is thus established immediately downstream of the injector.

Figure 9 shows the instantaneous distribution of the flame index in the injector near-field and downstream regions. Here the flame index, defined as: $G_{FO} = \nabla Y_F \nabla Y_O$, is used to distinguish premixed flames from diffusion flames, according to Yamashita et al. [53]. A positive value of G_{FO} represents a premixed flame while a negative value represents a diffusion flame. The overall flame is diffusion-dominated since the flame index is negative in most areas. The flame can be viewed as an ensemble of laminar diffusion flamelets that are stretched and contorted by the turbulent flow. These flamelets occur at local instantaneous stoichiometric surfaces. Figure 10 shows the temporal evolution of the flame field, with stoichiometric surfaces denoted by solid curves. The flame is anchored at the lower tip of the LOX post, above which is the kerosene-rich mixture. The stoichiometric surfaces are corrugated by vortical motions with a variety of sizes. The local strain rate imposed on the flamelets ($a_l \leq 1.2 \times 10^6$/s) is smaller than the extinc-

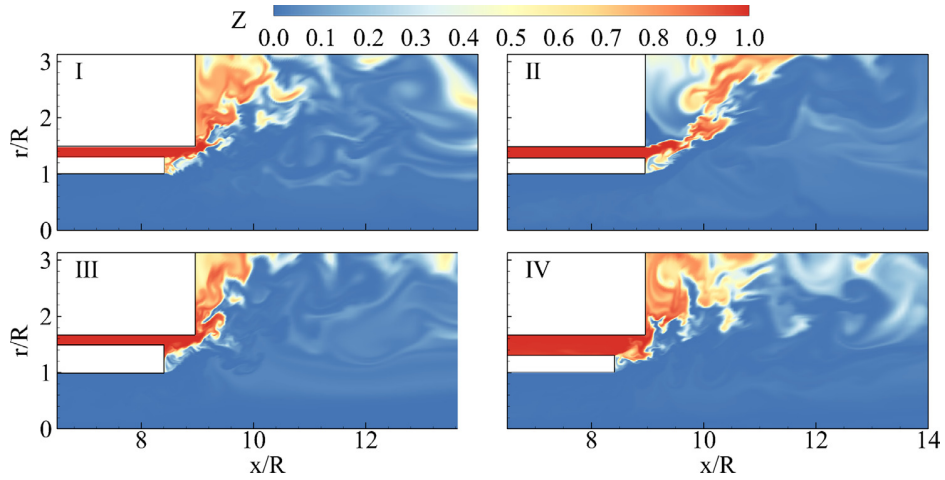

Fig. 11. Instantaneous distributions of the mixture fraction near the injector exit for all cases.

tion value ($\sim 10^7$/s) obtained for oxygen/kerosene counterflow diffusion flames. This may explain the presence of an anchored flame at the tip of the LOX post, rather than a liftoff flame for which the tip strain rate would exceed the extinction value [54]. If the exit velocities of the inner and outer swirlers increase, the local strain rate could exceed the extinction value, leading to unsteady effects and flame quenching.

4.2. Effect of injector geometry

Geometric parameters, including recess region, LOX post thickness, and kerosene annulus width, were identified in our cold-flow study [32] as important determinants of flow mixing characteristics. The presence of a recess region advances propellant interaction and improves mixing efficiency. A thicker post of the inner swirler or a wider annulus of the outer swirler leads to a larger spreading angle of the inner LOX film and intercepts the outer kerosene film in a broader area, thereby enhancing mixing in the recess region. Either of these changes may, however, reduce the thermal protection of the post in the combustion case, because the kerosene mass fraction along the post surface decreases. The effects of these geometric parameters on the combustion characteristics are examined in this section.

Figure 11 shows instantaneous distributions of the mixture fraction for all cases. The interaction of LOX and kerosene occurs internally in the recess region for Cases I, III, and IV. This interaction is, however, delayed to the downstream region for Case II (without recess). The corresponding kerosene stream penetrates further in the axial direction, in contrast to other cases in which the kerosene stream expands along the faceplate. The lack of kerosene coverage on the faceplate can impose significant heat flux on the surface. Figure 12 presents the distributions of the time-averaged temperature along the faceplate surface for all cases. The surface temperature in Case II is significantly higher than in the other cases. It strongly increases the need for cooling and reduces the injector lifespan. In comparison, Case IV has the lowest temperature distribution and thus provides the best thermal protection to the faceplate.

The temperature distribution provides direct insight into the flame characteristics. Figure 13 shows a snapshot of the temperature field near the recess region for all cases. The flame is slightly lifted off the LOX post for Cases I and II, with a thin flamelet attached to the lower post tip as shown in Fig. 10. For Case III, with an increased post thickness, the flame is anchored on the lower part of the post surface. A thicker post allows for larger recirculation zones in the recess region and provides a broader region for reactant mixing. Combustion efficiency is thus improved. Direct exposure of the post surface to the hot products, however, aggravates thermal loading, which is not desirable from the practical design perspective. The situation becomes even worse for Case IV, with a larger annulus width; the flame covers the entire back surface of the post. This is further demonstrated by the temperature and mixture-fraction distributions along the LOX post surface shown in Fig. 14. The peak value near the lower post tip ($r/R = 1.0$) indicates the presence of a thin flamelet, which corresponds to the stoichiometric mixture fraction ($Z_{st} = 0.225$). The temperature then decreases while the mixture fraction increases along the radial direction. Case I has the lowest temperature on the post surface, followed by Cases II and III, and Case IV shows the strongest thermal distribution ($\sim$1800 K) and would require extreme care in cooling if it were used in practical systems.

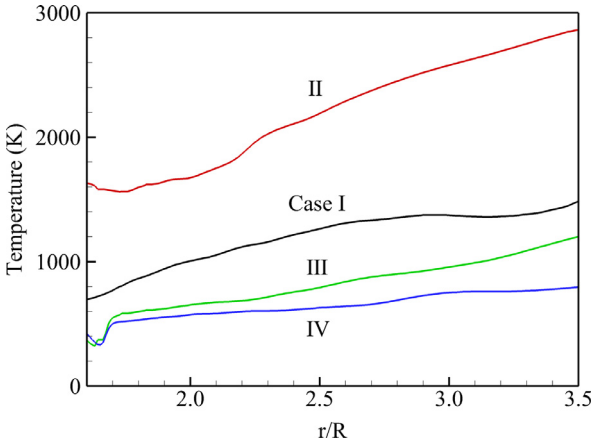

Fig. 12. Distributions of time-averaged temperature along the faceplate surface for all cases.

The distribution of mixture fraction shows the opposite trend. It is the largest for Case I and the lowest for Case IV. All these cases are kerosene-rich along the post surface ($r/R > 1.1$). A richer value corresponds to better thermal protection, but it is less able to stabilize the flame in this zone during extreme events such as high strain rates. Note that in the present study the adiabatic boundary condition is enforced at solid surfaces. The flame is inclined to anchor closely to the post surface. In practical problems with heat losses, the flame may be slightly lifted off in Cases III and IV, and

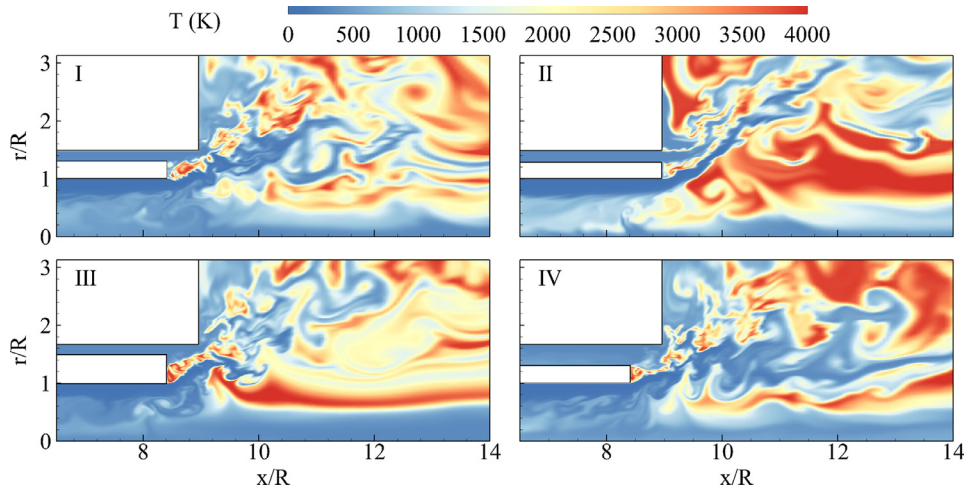

Fig. 13. Snapshot of the temperature field near the injector exit for all cases.

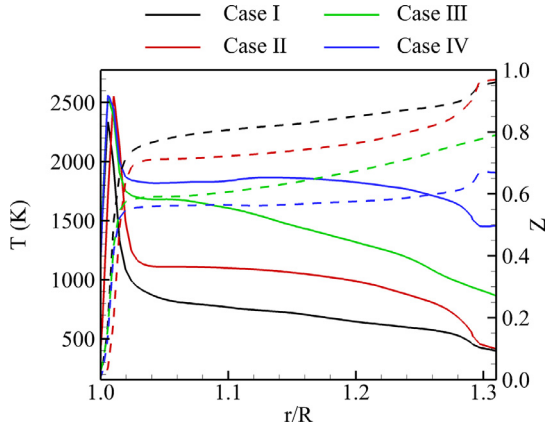

Fig. 14. Radial distributions of time-averaged temperature (solid lines) and mixture fraction (dashed lines) along the back surface of the LOX post.

the liftoff height for Cases I and II becomes larger than their counterpart in the present study. The comparative discussion here offers useful information on the impact of the geometric parameters on the injector performance.

Figure 13 also shows a high-temperature zone beneath the LOX film at the injector exit for all cases. This zone is in the center-recirculating region and plays an important role in preheating the incoming LOX and sustaining the flame downstream. It is interesting to explore what the composition is in this zone and whether unburnt kerosene is present to react with oxygen to induce the high-temperature zone. As an example, the instantaneous distributions of the major species mass fractions and the volumetric heat release rate in the injector near field are presented in Fig. 15 for Case III. In this zone oxygen-rich hot products are present, primarily consisting of oxygen, water, and CO_2. Some of the water and CO_2 are carried from the downstream flame zone and transported to the recirculating zone. A significant portion of CO_2 comes from the further oxidization of CO. This is manifested by the relatively low concentration of CO in the recirculation zone. The H and OH radicals that are generated during CO oxidation promote the production of water. The recirculation region is thus dominated by exothermic reactions with strong heat release as shown in Fig. 15. Kerosene is confined in the annulus and along the faceplate, where endothermic reactions with heat absorption are significant because of thermal decomposition. This in return protects the faceplate thermally by diminishing the heat flux.

Figure 16 shows time-averaged streamlines near the injector exit. Two counter-rotating vortices form in the wake of the LOX post for all cases. The radial span of the vortices is comparable to the post thickness for Cases I–III. The LOX post of Case III is 0.5 mm thicker, and produces larger vortices and enhanced propellant mixing. This explains the distributions of lower mixture fraction and higher temperature in Fig. 14. The flow pattern for Case IV is more complicated. The radial span of the vortices is larger than the post thickness, and the upper vortex expands into the kerosene stream. A small recirculating zone appears on the lower surface of the kerosene annulus. Although this unique pattern improves mixing and flame stabilization, it introduces unstable combustion behaviors. Vortex rollup transports the oxidizer to the small recirculation zone surrounded by kerosene, giving rise to unsteady combustion in this region [31].

Figure 17 shows the time history of the relative pressure (p'/p_0) oscillations probed in the flame zone near the injector exit, where there is a strong shear layer between the LOX and kerosene streams. Limit cycles appear for all cases, but the amplitude of these fluctuations varies with different geometric parameters. The maximum pressure fluctuations for Cases II and IV reach a high amplitude, sufficient to cause system damage. In contrast, the peak values for Cases I and III are relatively small (<5%). Figure 18 shows the frequency spectra of these pressure fluctuations to offer insight into the characteristic frequencies dictating flow oscillations. The dominant frequency is very similar for Cases I, III, and IV (~6.47 kHz), corresponding to the vortex shedding frequency in the wake region of the LOX post. This frequency characterizes the flow instability produced by the interaction between the shear layer issuing from the inner swirler and the shear layer issuing from the kerosene annulus, and is determined by the exit velocity profile [13]: $f_v = StU/\theta$, where St and θ are Strouhal number and momentum thickness, respectively. Since Cases I, III and IV have similar exit velocity profiles, the characteristic frequencies for these cases are similar, as shown in Fig. 18. For Case II (without recess), the dominant pressure oscillations occur at a higher frequency (19.6 kHz) with relatively small amplitude. This difference from the other cases might be caused by the deviation in the exit velocity profile of the kerosene annulus for Case II, which is manifested by longer axial penetration, as shown in Fig. 11. This induces a different shear layer and vortex interactions, compared to the other cases with recess region. The corresponding recirculation zone near the injector faceplate (Fig. 16) is broader.

Another prominent peak in the frequency spectra occurs at 4.89 kHz for Case I. This corresponds to the characteristic fre-

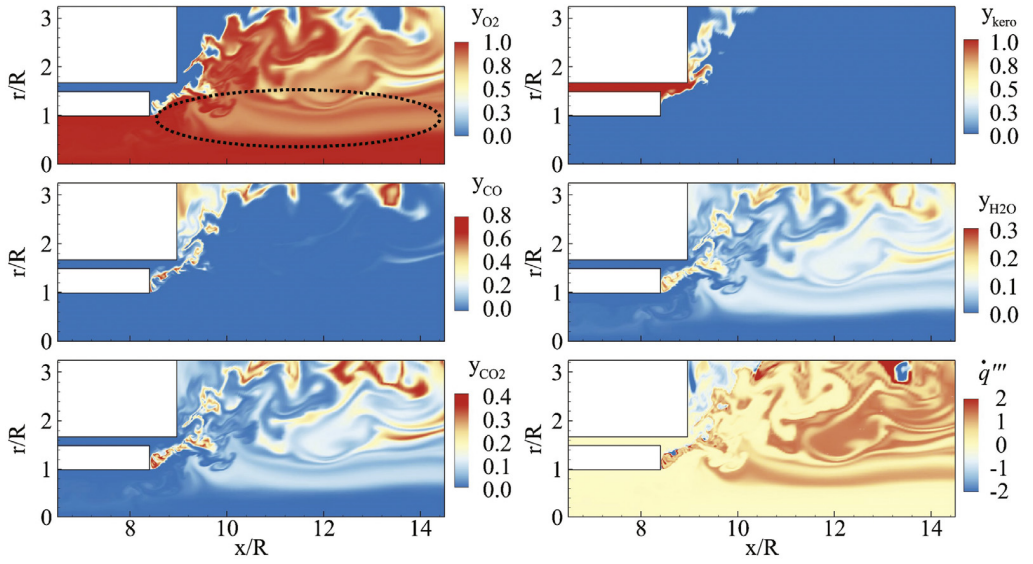

Fig. 15. Instantaneous distributions of the major species mass fractions and the volumetric heat release rate (100 kW/cm^3) for Case III.

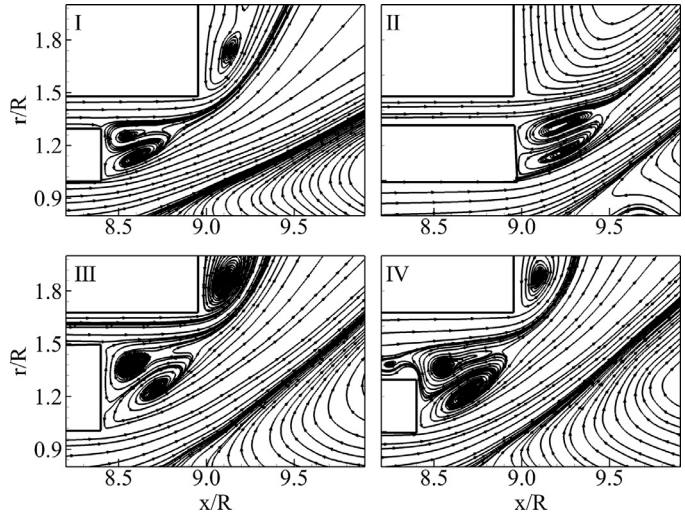

Fig. 16. Time-averaged streamlines near the injector exit for all cases.

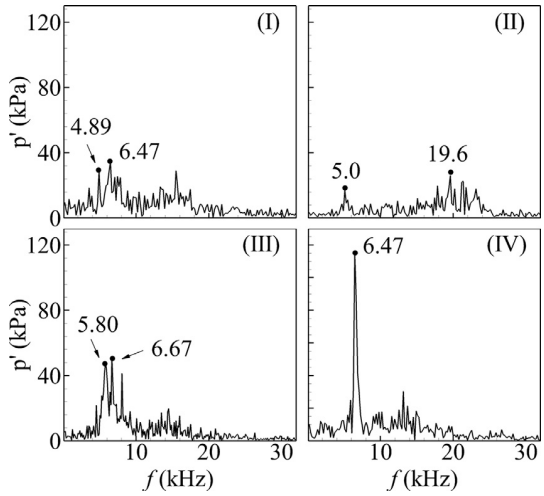

Fig. 18. Frequency spectra of pressure oscillation in the flame zone for all cases.

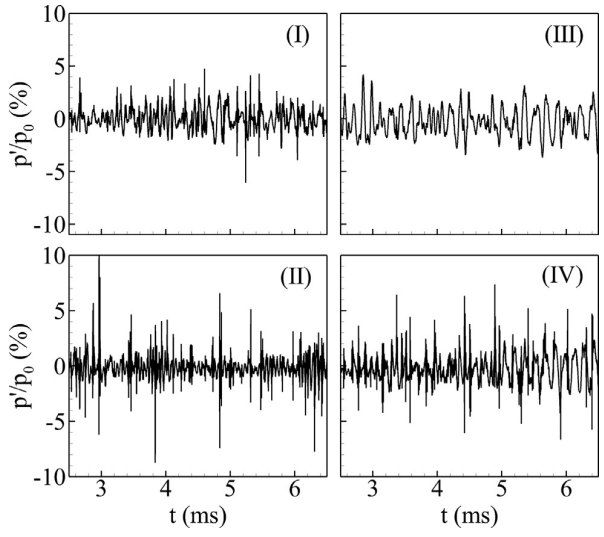

Fig. 17. Temporal evolution of pressure oscillation in the flame zone for all cases.

quency (f_a) of the acoustic wave in the inner swirler. Earlier work [13] indicated that the inner swirler can be acoustically treated as a quarter-wave resonator, with a closed head end and an open exit. The fundamental frequency is empirically determined by $f_a = c/4(L + \Delta l)$, where c, L, and Δl represent the speed of sound, length of the inner swirler, and a correction factor, respectively. Following the empirical approach, a value of 4.8 kHz was obtained in the earlier work for the non-reacting flow [13]. A slightly larger value (4.89 kHz for Case I) is expected in the present study, because the speed of sound in the inner swirler is enhanced, due to the flow reversal of hot combustion products. The temperature of the gaseous core for Cases II and III is even higher than that for Case I, leading to higher sound speed and acoustic frequency (5.0 kHz for Case II and 5.8 kHz for Case III). Note that vortex shedding overshadows the acoustic wave for Case IV at the injector exit, but these acoustic motions play a more dominant role within the injector, where the effect of vortex motions is small. The acoustic waves in the injector are closely coupled with the fluctuations of heat release rate in the downstream region. The dynamic responses between acoustic and flame interactions can be described by a flame transfer function, which is relatively new for non-premixed

flame [55]. A detailed solution to obtain the flame transfer function using advanced statistical regression models will be presented in subsequent work.

5. Conclusion

The flame dynamics of LOX/kerosene bi-swirl injectors were numerically investigated at supercritical pressure using the large eddy simulation technique. The physical model and flow conditions mimic the RD-0110 engine injectors. The theoretical and numerical framework is implemented using a unified treatment of the general fluid thermodynamic and transport properties. Turbulence/chemistry modeling is handled with a laminar flamelet library approach, which is justified by the fact that the local flow strain rate is an order of magnitude smaller than the extinction value. The flame is found to be anchored near the post surface of the inner LOX swirler by two counter-rotating vortices. The corresponding flow residence time is longer than the ignition delay time after the flame is initiated by the flamelet library, so sustainable flame holding is found in the wake region of the LOX post. The intensive burning is further stabilized by the center and corner recirculation zones in the downstream region.

The effects of injector geometric parameters, including the recess region, LOX post thickness, and kerosene annulus width, on flame characteristics have been explored. The presence of the recess region advances propellant mixing and enhances the radial expansion of the kerosene stream, which tends to flow along the injector faceplate and thus provides thermal protection from the hot products. Increasing the post thickness or the annulus width can further improve such thermal protection. Both changes in geometry also induce larger recirculation flows in the wake region of the post, and thus better stabilize the flame. These advantages bear the price of higher temperature distribution against the post surface, which aggravates the surface thermal load.

The dynamic characteristics of the flame field have also been investigated. The injector can be acoustically treated as a quarter-wave resonator, whose frequency varies with different geometries because of the difference in the temperature of the gaseous core. The vortex shedding induced by the inner and outer shear layers near the injector exit plays a prominent role in flame dynamics. The characteristic frequency is determined by the exit velocity distribution and is similar for different post thicknesses and annulus widths. The case without a recess region shows a different velocity profile and vortex interactions. The recess length, post thickness, and annulus width must be carefully selected in the process of injector design to achieve optimal injector performance.

For the future work, a full 3D simulation should be performed to examine the transverse flow instabilities and their interactions with longitudinal ones. The sensitivity of wall heat transfer, SGS models, and combustion model to the flow structures and flame evolution should be investigated at supercritical conditions.

Acknowledgments

This work was sponsored partly by the Air Force Office of Scientific Research under grant no. FA 9550-10-1-0179, and partly by the William R. T. Oakes Endowment of the Georgia Institute of Technology. The authors gratefully acknowledge support and advice given by Mitat A. Birkan.

References

[1] V.R. Rubinsky, Instability phenomenology and case studies: combustion instability in the RD-0110 engine, in: V. Yang, W.E. Anderson (Eds.), Liquid Rocket Engine Combustion Instability, Progress in Astronautics and Aeronautics, 169, AIAA (1995), pp. 89–112.
[2] Y. Huang, V. Yang, Dynamics and stability of lean-premixed swirl-stabilized combustion, Prog. Energy Combust. Sci. 35 (2009) 293–364.
[3] T.C. Lieuwen, V. Yang (Eds.), Combustion instabilities in gas turbine engines (operational experience, fundamental mechanisms and modeling), Progress in Astronautics and Aeronautics, 210, AIAA (2005).
[4] V.G. Bazarov, V. Yang, Liquid-propellant rocket engine injector dynamics, J. Propul. Power 14 (1998) 797–806.
[5] V. Bazarov, V. Yang, P. Puri, Design and dynamics of jet and swirl injectors, in: V. Yang, M. Habiballah, J. Hulka, M. Popp (Eds.), Liquid Rocket Thrust Chambers: Aspects of Modeling, Analysis, and Design, Progress in Astronautics and Aeronautics, AIAA (2004), pp. 19–103. 200.
[6] W.-W. Kim, S. Menon, H.C. Mongia, Large-eddy simulation of a gas turbine combustor flow, Combust. Sci. Technol. 143 (1999) 25–62.
[7] Y. Huang, S. Wang, V. Yang, Systematic analysis of lean-premixed swirl-stabilized combustion, AIAA J. 44 (2006) 724–740.
[8] P. Moin, S.V. Apte, Large-eddy simulation of realistic gas turbine combustors, AIAA J. 44 (2006) 698–708.
[9] S. Wang, V. Yang, G. Hsiao, S.-Y. Hsieh, H.C. Mongia, Large-eddy simulations of gas-turbine swirl injector flow dynamics, J. Fluid Mech. 583 (2007) 99–122.
[10] V. Yang, Modeling of supercritical vaporization, mixing, and combustion processes in liquid-fueled propulsion systems, Proc. Combust. Inst. 28 (2000) 925–942.
[11] Q.-F. Fu, L.-J. Yang, X.-d. Wang, Theoretical and experimental study of the dynamics of a liquid swirl injector, J. Propul. Power 26 (2010) 94–101.
[12] N. Zong, V. Yang, Cryogenic fluid dynamics of pressure swirl injectors at supercritical conditions, Phys. Fluids 20 (2008) 056103.
[13] X. Wang, H. Huo, Y. Wang, V. Yang, Comprehensive study of cryogenic fluid dynamics of swirl injectors at supercritical conditions, AIAA J. 55 (9) (2017) 3109–3119.
[14] M. Sasaki, H. Sakamoto, M. Takahashi, T. Tomita, H. Tamura, Comparative study of recessed and non-recessed swirl coaxial injectors, AIAA Paper (1997) 2907.
[15] P.-G. Han, J. Seol, S. Hwang, Y. Yoon, The spray characteristics of swirl coaxial injectors, AIAA Paper (2003) 490.
[16] T. Inamura, H. Tamura, H. Sakamoto, Characteristics of liquid film and spray injected from swirl coaxial injector, J. Propul. Power 19 (2003) 632–639.
[17] M. Soltani, K. Ghorbanian, M. Ashjaee, M. Morad, Spray characteristics of a liquid–liquid coaxial swirl atomizer at different mass flow rates, Aerosp. Sci. Technol. 9 (2005) 592–604.
[18] Q.-F. Fu, L. Yang, Y.-Y. Qu, B. Gu, Geometrical effects on the fluid dynamics of an open-end swirl injector, J. Propul. Power 27 (2011) 929–936.
[19] R.J. Kenny, J.R. Hulka, M.D. Moser, N.O. Rhys, Effect of chamber backpressure on swirl injector fluid mechanics, J. Propul. Power 25 (2009) 902–913.
[20] X. Chen, V. Yang, Effect of ambient pressure on liquid swirl injector flow dynamics, Phys. Fluids 26 (2014) 102104 (1994-present).
[21] K. Ahn, Y.-M. Han, S. Seo, H.-S. Choi, Effects of injector recess and chamber pressure on combustion characteristics of liquid–liquid swirl coaxial injectors, Combust. Sci. Technol. 183 (2010) 252–270.
[22] K. Ahn, Y.-M. Han, H.-S. Choi, Effects of recess length on discharge coefficients of swirl coaxial injectors, Combust. Sci. Technol. 184 (2012) 323–336.
[23] N.A. Okong'o, J. Bellan, Direct numerical simulation of a transitional supercritical binary mixing layer: heptane and nitrogen, J. Fluid Mech. 464 (2002) 1–34.
[24] P.E. Lapenna, F. Creta, Mixing under transcritical conditions: an a-priori study using direct numerical simulation, J. Supercrit. Fluids 128 (2017) 263–278.
[25] L.C. Selle, N.A. Okong'o, J. Bellan, K.G. Harstad, Modelling of subgrid-scale phenomena in supercritical transitional mixing layers: an a priori study, J. Fluid Mech. 593 (2007) 57–91.
[26] H. Huo, X. Wang, V. Yang, A priori analysis of SGS models for large-eddy simulation of supercritical mixing and combustion, AIAA J. Submitted (2017).
[27] J.C. Oefelein, Large eddy simulation of turbulent combustion processes in propulsion and power systems, Progr. Aerosp. Sci. 42 (2006) 2–37.
[28] T. Schmitt, Y. Méry, M. Boileau, S. Candel, Large-eddy simulation of oxygen/methane flames under transcritical conditions, Proc. Combust. Inst. 33 (2011) 1383–1390.
[29] H. Huo, V. Yang, Large-eddy simulation of supercritical combustion: model validation against gaseous H_2–O_2 injector, J. Propul. Power 33 (2017) 1272–1284.
[30] P.C. Ma, Y. Lv, M. Ihme, An entropy-stable hybrid scheme for simulations of transcritical real-fluid flows, J. Comput. Phys. 340 (2017) 330–357.
[31] X. Wang, V. Yang, Supercritical mixing and combustion of liquid-oxygen/kerosene bi-swirl injectors, J. Propul. Power 33 (2017) 316–322.
[32] X. Wang, Y. Wang, V. Yang, Geometric effects on liquid oxygen/kerosene bi-swirl injector flow dynamics at supercritical conditions, AIAA J. 55 (10) (2017) 3467–3475.
[33] J.C. Oefelein, V. Yang, Modeling high-pressure mixing and combustion processes in liquid rocket engines, J. Propul. Power 14 (1998) 843–857.
[34] G. Erlebacher, M. Hussaini, C. Speziale, T.A. Zang, Toward the large-eddy simulation of compressible turbulent flows, J. Fluid Mech. 238 (1992) 155–185.
[35] S. Takahashi, Preparation of a generalized chart for the diffusion coefficients of gases at high pressures, J. Chem. Eng. Jpn. 7 (1975) 417–420.
[36] N. Zong, H. Meng, S.Y. Hsieh, V. Yang, A numerical study of cryogenic fluid injection and mixing under supercritical conditions, Phys. Fluids 16 (2004) 4248–4261.
[37] H. Huo, X. Wang, V. Yang, A general study of counterflow diffusion flames at subcritical and supercritical conditions: oxygen/hydrogen mixtures, Combust. Flame 161 (2014) 3040–3050.

[38] X. Wang, H. Huo, V. Yang, Counterflow diffusion flames of oxygen and n-alkane hydrocarbons (CH_4-$C_{16}H_{34}$) at subcritical and supercritical conditions, Combust. Sci. Technol. 187 (2015) 60–82.
[39] H. Huo, V. Yang, Subgrid-scale models for large-eddy simulation of supercritical combustion, AIAA Paper (2013) 706.
[40] U. Unnikrishnan, X. Wang, S. Yang, V. Yang, Subgrid scale modeling of the equation of state for turbulent flows under supercritical conditions, AIAA Paper (2017) 4855.
[41] X. Petit, G. Ribert, P. Domingo, Framework for real-gas compressible reacting flows with tabulated thermochemistry, J. Supercrit. Fluids 101 (2015) 1–16.
[42] G. Ribert, X. Petit, P. Domingo, High-pressure methane-oxygen flames. Analysis of sub-grid scale contributions in filtered equations of state, J. Supercrit. Fluids 121 (2017) 78–88.
[43] T. Poinsot, D. Veynante, Theoretical and numerical combustion, RT Edwards, Inc., 2005.
[44] P. Dagaut, A. El Bakali, A. Ristori, The combustion of kerosene: experimental results and kinetic modelling using 1-to 3-component surrogate model fuels, Fuel 85 (2006) 944–956.
[45] Q.-D. Wang, Y.-M. Fang, F. Wang, X.-Y. Li, Skeletal mechanism generation for high-temperature oxidation of kerosene surrogates, Combust. Flame 159 (2012) 91–102.
[46] R.J. Kee, F.M. Rupley, J.A. Miller, II Chemkin, A Fortran Chemical Kinetics Package for the Analysis of Gas-Phase Chemical Kinetics, Sandia National Labs., Livermore, CA (USA), 1989.
[47] H. Meng, V. Yang, A unified treatment of general fluid thermodynamics and its application to a preconditioning scheme, J. Comput. Phys. 189 (2003) 277–304.
[48] S.-Y. Hsieh, V. Yang, A preconditioned flux-differencing scheme for chemically reacting flows at all Mach numbers, Int. J. Comput. Fluid Dyn. 8 (1997) 31–49.
[49] R.C. Swanson, E. Turkel, On central-difference and upwind schemes, J. Comput. Phys. 101 (1992) 292–306.
[50] A.M. Ruiz, G. Lacaze, J.C. Oefelein, R. Mari, B. Cuenot, L. Selle, T. Poinsot, Numerical benchmark for high-Reynolds-number supercritical flows with large density gradients, AIAA J. 54 (2015) 1445–1460.
[51] H.-G. Li, N. Zong, X.-Y. Lu, V. Yang, A consistent characteristic boundary condition for general fluid mixture and its implementation in a preconditioning scheme, Adv. Appl. Math Mech. 4 (2012) 72–92.
[52] N. Zong, H. Meng, S.Y. Hsieh, V. Yang, A numerical study of cryogenic fluid injection and mixing under supercritical conditions, Phys. Fluids 16 (2004) 4248.
[53] H. Yamashita, M. Shimada, T. Takeno, A numerical study on flame stability at the transition point of jet diffusion flames, Symp. (Int.) Combust. 26 (1996) 27–34.
[54] N. Peters, F.A. Williams, Liftoff characteristics of turbulent jet diffusion flames, AIAA J. 21 (1983) 423–429.
[55] Y. Li, X. Wang, S. Mak, S.-T. Yeh, L.-H. Lin, C.-F.J. Wu, V. Yang, A two-stage transfer function identification methodology and its applications to bi-swirl injectors, AIAA Paper (2017) 4933.